Original article

Citrate-silver nanoparticles and their impact on some environmental beneficial fungi

Lacramioara Oprica [a], Maria Andries [b], Liviu Sacarescu [c], Larisa Popescu [b], Daniela Pricop [b], Dorina Creanga [b,*], Maria Balasoiu [d]

[a] Alexandru Ioan Cuza" University, Faculty of Biology, Blvd. Carol I, 11 A, Iasi, Romania
[b] Alexandru Ioan Cuza" University, Faculty of Physics, Blvd. Carol I, 11 A, Iasi, Romania
[c] Petru Poni Institute of Macromolecular Chemistry, Iasi, Romania
[d] Frank Laboratory of Neutron Physics, Joint Institute for Nuclear Research, Joliot-Curie 6, Dubna, 141980, Moscow Region, Russian Federation

ABSTRACT

Colloidal suspensions of silver nanoparticles (AgNPs) with surface modified by capping with citrate ions were synthesized by chemical reduction method. Transmission and Scanning Electron Microscopy as well as darkfield Optical Microscopy provided information on the nanoparticle morphology, with fine symmetrical grains and log-normal fitted size distribution. Small Angle X-ray Scattering method allowed theoretical confirmation of colloidal silver nanoparticle fine granularity, based on measurements in the native fluid sample. UV–Vis spectrophotometry allowed studying the Localized Surface Plasmon Resonance band versus the stability of the citrate-AgNP sample after storage and after UV-C exposure. The colloidal AgNP impact on *Phanerochaete chrysosporium* environmental microorganisms was studied by specific biochemical investigations. Silver released from the colloidal suspension of AgNPs was supposed to induce changes in some antioxidant enzymes and in some enzymes of Krebs' cycle. Catalase activity was moderately changed (an increase with over 50%) as well as superoxide dismutase activity, while the diminution of the activities of four dehydrogenases synthesized in the *fungus mycelium* was emphasized also: a decrease with about 60% for malate dehydrogenase, with over 50% for isocitrate dehydrogenase and succinate dehydrogenase and with about 40% for alpha-ketoglutarate dehydrogenase. These findings suggested the nano-toxicological issues of citrate-AgNPs impact on the environmental beneficial microorganisms.

© 2020 The Authors. Published by Elsevier B.V. on behalf of King Saud University. This is an open access article under the CC BY-NC-ND license (http://creativecommons.org/licenses/by-nc-nd/4.0/).

1. Introduction

Nanoparticulate matter, mainly metal nanoparticles, is related to tremendous application arrays in electronics, chemical industries, space industries, medicine, pharmaceutics, cosmetics, optics, biology, drug delivery, catalysis, light emitters and others (Vicky et al., 2010). All nanosized particles are characterized by specific physical and chemical features, remarkably changed compared to the bulk metals, due to exceptionally high surface-to-volume ratio. The intensive exploration of the silver nanoparticles (AgNPs) as well as of the gold ones was determined by their special behavior, mainly in the optical domain, that empowered important development of optoelectronics and sensing device techniques (Lee and Jun, 2019; Sharma et al., 2018; Chettri et al., 2017; Jeong et al., 2015).

The AgNP formation in the reaction medium is indicated by the light absorption peak denoting the occurrence of the Localized Surface Plasmon Resonance (LSPR) phenomenon. LSPR, as an optical characteristic of noble metal nanoparticles, is understood in the terms of collective coherent oscillations of free electrons from metal particles surface following resonant interaction with incident light. LSPR peak position on the wavelength scale is often described as dependent on the nanoparticle size and shape as well as being related to the molecular neighboring, i.e. pH, refractive index and agglomeration/assembly state (Mahmudin et al., 2015; Amendola et al., 2010; Cao et al., 2011).

* Corresponding author.
E-mail address: mdor@uaic.ro (D. Creanga).

Peer review under responsibility of King Saud University.

Production and hosting by Elsevier

Due to the localized surface plasmon resonance effect, AgNPs have been used, for example, to color merino wool fibers, leading to novel AgNP-wool composite materials with different colors depending on AgNP size and their interaction with keratin from wool fibers (Kelly and Johnston, 2011); nevertheless disinfectant features have been conferred to those fabrics (Pietrzak et al., 2016). Numerous applications were developed in the life sciences research, based on AgNPs as source of silver, such as in pharmacy, cosmetics, sanitation, wastewater treatment, etc., (Tylkowski et al., 2017; Bapat et al., 2018; Kaur et al., 2018; Huang et al., 2020; Al-Zubaidi et al., 2019; Osonga et al., 2020; Bernardo-Mazariegos,et al., 2019). Generally silver ions were found to be the actual active agent, when released from silver nanoparticles (AgNPs) – since there is no final statement that nanoparticles themselves have antimicrobial or antifungal activity (Ivask et al., 2014; Mittelman et al., 2015)). In the U.S. alone, in 2011 the production of minimum 2.8 t of AgNPs was estimated with enhanced perspective for 2025 (up to 800 t) (Calderón-Jiménez et al., 2017) meaning huge amount of particles released in the environment. Various fungi strains (Zhao et al., 2018) were found able to have a high tolerance to metals and to secrete extracellular proteins suitable to stabilize the AgNPs. Some examples of such fungi can be given, like *Aspergillus flavus* (Vigneshwaran et al., 2007), *Trichoderma reesei* (Vahabi et al., 2011), *Phanerochaete chrysosporium* (Kobashigawa et al, 2019).

Significant number of published papers have focused on silver nanotoxicity in fungal cells. The influence of AgNPs, produced by the high-voltage arc discharge, on the worldwide spread spores of *Fusarium* soil fungus, was shown in the report of Kasprowicz et al. (2010) where significant diminution of mycelial growth was found because of silver nanotoxicity. Alananbeh et al. (2017) have supplied with uncoated AgNPs the culture medium of filamentous fungi, found in soil and the decaying vegetation, demonstrating the growth inhibition to the increase of AgNPs concentration. Special attention was paid to the response of beneficial microorganisms from the biosphere to the AgNP pollution, like in the case of the cellulolytic fungus *Phanerochaete chrysosporium*, able to decompose wood wastes from natural and anthropogenic sources; recent studies evidenced also its contribution to plastic waste degrading (Gutierrez et al., 2015). Yi et al. (2016) described the reactive oxygen species (ROS) formation in *P. chrysosporium* when supplied with citrate-coated AgNPs; Huang et al. (2017) studied the silver nanoparticles and silver ions from the viewpoint of their influence on the capacity of *P. chrysosporium* to degrade the dichlorophenol, emphasizing the role of extracellularly released silver ions. Another study (Huang et al., 2018) revealed the roles of antioxidant enzymes, among which the catalase and superoxide dismutase, in reducing lipid degrading by reactive oxygen species in the *P. chrysosporium* supplied with nanoparticulate silver.

In our laboratory we studied the synthesized citrate-silver colloidal nanoparticles, their stability properties and their impact on some biotic components of environment represented by cellulolytic fungus *P. chrysosporium*, which was tested at biochemical level for some enzyme activities.

2. Methods

2.1. Colloidal silver nanoparticle synthesis

2.1.1. Materials and methods

Reagents. The reagents we used were silver nitrate (AgNO$_3$ from Merck Chemical Company), as precursor salt, and dihydrated trisodium citrate (Na$_3$C$_6$H$_5$O$_7$ × 2H$_2$O from Sigma Aldrich), as reducing and capping agent. The colloidal silver nanoparticles were prepared by applying basically the chemical reduction method described by Lee and Meisel (1982). All reagent solutions were prepared using Milli-Q deionized water (18.2 MOhm).

Phanerochaete chrysosporium L., belonging to fungi strain collection of Biology Faculty of "Alexandru Ioan Cuza" University in Iași, Romania was achieved from the Institute Scientifique de Santé Publique, Belgium (HEM no. 5772). Its role in the environment is to decompose wood waste from biosphere.

Synthesis protocol. 50 ml of 1 mM AgNO$_3$ were heated in an Erlenmeyer flask. When the temperature was close to the boiling point, to this solution, 5 ml of 1% trisodium citrate were carefully added drop by drop. During the process, vigorously mixing was carried out to ensure the increased interaction of the reagents, the reaction vessel being kept on a heating plate at over 60 °C, until its color changed from uncolored to pale yellow, suggesting the formation of AgNPs. At this very moment the reaction vessel was removed from the heating device while the stirring has continued until the room temperature was reached. The mechanism of reduction reaction could be expressed as follows (Silva et al., 2007):

$$4Ag^+ + C_6H_5O_7Na_3 + 2H_2O \rightarrow 4Ag^0 + C_6H_5O_7H_3 + 3Na^+ + H^+ + O_2\uparrow \tag{1}$$
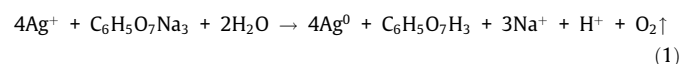
The reduced silver, Ag^0, forms AgNPs with citrate attached to the surface, and dispersed in aqueous medium. The as-prepared colloidal silver suspension was studied from the viewpoint of physical characteristics and some biological effects, and also from the viewpoint of its stability in time and under UV exposure.

2.1.2. Sample ageing and UV exposure

The synthesized citrate-AgNP colloidal suspension was stored for one year in darkness, coated in black paper, in a refrigerator (5 °C) with non-transparent walls and doors, and after that the sample was exposed to UV-C, by using a 30 W bactericidal lamp, emitting radiations in the range 100–280 nm.

The UV lamp, a Philips brand, was a low pressure mercury vapor discharge tube emitting UV-C radiation with a peak at 253.7 nm (mercury line); glass tube filters out the 185 nm ozone – forming line. The total UV power was of 30 W while the UV-C radiation power was of 12 W, according to producer specifications.

The exposure was carried out on 10 ml of aged silver sample in a 3 cm diameter vessel at 25 cm under the center of the horizontal radiation tube for 100 min. The formula provided by Keitz (Sasges et al., 2012) allowed the calculation of the irradiance, I (W/m^2) under the horizontal tube center, at the distance D as:

$$P = I.2\pi^2 DL/(2\alpha + \sin 2\alpha) \tag{2}$$
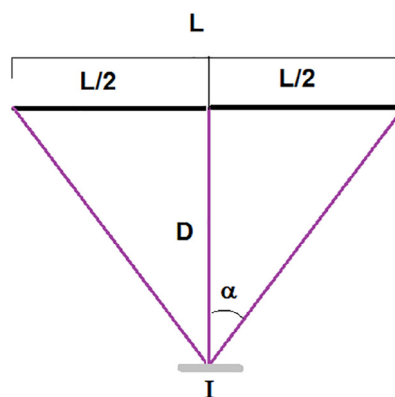
Scheme 1. UV tube lamp, with the length *L*, emitting at the central point (the distance *D*), the irradiance *I* (W/m^2), under the angle α.

where L is the tube length and α is the angle represented in the Scheme 1 (in radians).

In the case of our experimental arrangement, D = 0.25 m, L = 0.87 m, as measured, and P is given by the producer as 12 W for the UV-C radiation; the angle α has resulted to be equal to about $\pi/3$ rad; thus we worked with the calculated irradiance, I, resulted from formula (2), of 26.22 W/m^2, in the center of the exposed sample:

$$I = P(2\alpha + \sin 2\alpha)/(2\pi^2 DL) \qquad (3)$$

The total UV-C energy delivered at that point is equal to the irradiance $\times$ exposure time; we might consider that the diameter of the vessel containing the sample, of 0.03 m, is much smaller than the values of L and D, thus it can be assumed that the irradiance is that calculated in the central point. The total energy the sample was exposed to, resulted as equal to 43.5 J. The results can be considered reliable with ±5% accuracy and have shown good agreement with goniometric measurements (Lawal et al., 2017).

2.2. Sample characterization

The Transmission Electron Microscopy (TEM), using model Hitachi High-Tech HT7700 device, with energy-dispersive X-ray analysis (EDX) module (HV of 100.0 kV, range 20 keV/130 kcps), was utilized to evidence particle morphology and size distribution.

The small-angle X-ray scattering (SAXS) experiments were performed on a Nanostar U-Bruker system equipped with a Vantec 2000 detector (diameter of 200 mm) and an X-ray I μS microsource. The wavelength of the incident X-ray beam was λ = 1.54 Å (Cu Kα line), and the beam was collimated by three pinholes. The scattered intensity $I(q)$ was plotted as a function of the momentum transfer vector $q = 4\pi \sin \theta/\lambda$, where λ is the wavelength of the X-rays and 2θ is the scattering angle. The sample-to-detector distance was 107 cm allowing measurements with q values between 0.008 Å^{-1} and 0.3 Å^{-1}. The angular scale was calibrated by the scattering peaks of a silver behenate standard. The sample under study was sealed in a quartz capillary and measured under vacuum at constant temperature, 25 °C for 10000 s. The capillary and solvent backgrounds were subtracted from the original intensity profiles. The data analysis was done using the softwares: Bruker AXS software and "IRENA: tool suite for modeling and analysis of small-angle scattering", (Ilavsky and Jemian, 2009).

The optical properties of AgNP colloidal suspensions were evidenced with Shimadzu UV–VIS Pharma Spec 1700 spectrophotometer and Nikon Ti-Eclipse Optical Microscope working in darkfield (DF) mode.

2.3. Bioeffects investigation

2.3.1. Fungus growth test

Petri dishes with Sabouraud agarized culture medium (10 g/l peptone, 35 g/l glucose, 2 g/l agar, distilled water up to 1.0 (Manoliu et al., 2010)) were inoculated with 0.8 cm discs extracted from the 7 days old *Phanerochaete chrysosporium* agarized stock culture. The fungi growth was conducted in the presence of different AgNP suspension concentrations (experimental variants V1, V2, V3, V4, V5 – corresponding to different concentrations of silver suspension in the culture medium: 200–400-600–800-1000 µl/l, Table 1).

The control sample (C) was prepared identically except no silver source was supplied to the fungi culture medium. Five replies were arranged for each experimental variant.

2.3.2. Biochemical assay

2.3.2.1. Catalase, superoxide dismutase and malonedialdehyde.
The activities of antioxidant enzymes catalase (CAT) and superoxide dismutase (SOD) from the fungal mycelium were assayed according to literature (Sinha, 1972; Winterbourn et al., 1975) while malondialdehyde (MDA) content according to Hodges et al. (1999) was measured as indirect indicator of lipid peroxidation, for complementary interpretation of cellular oxidative stress. All reagents were purchased from Sigma Aldrich chemical company. A Shimadzu PharmaSpec 1700 spectrophotometer, provided with of 1 cm quartz cells and specialized soft for data acquisition and analysis was utilized. The activity of CAT enzyme, having as specific substrate the hydrogen peroxide, was assayed spectrophotometrically at λ = 570 nm by Sinha protocol (Sinha, 1972) based on the determination of chromium acid resulted by the reduction of $K_2Cr_2O_7$, in acidic medium, in the presence of non-decomposed H_2O_2. The SOD activity was assayed at 560 nm according to the adapted Winterbourn's protocol (Winterbourn et al., 1975), based on enzyme ability to inhibit the reduction of nitro blue tetrazolium (NBT) by means of superoxide radical generated in the reaction mixture through the photoreduction of the riboflavin. All samples were exposed to illumination for exactly 5 min using 20 W neon lamps at a distance of 10 cm. The assay of MDA, the secondary end product of the oxidation of polyunsaturated fatty acids and the general index of lipid peroxidation, was carried out using the thiobarbituric acid reactive substances (TBARS), according to the adapted protocol of Hodges (Hodges et al., 1999). The general method for measuring MDA was based on the light extinction at 532 nm, after MDA containing mycelium was let to react with the thiobarbituric acid (TBA).

2.3.2.2. Krebs' cycle dehydrogenases.
Krebs' cycle dehydrogenases' activities were estimated by the spectrophotometric assays at 540 nm, based on each enzyme capacity of transferring hydrogen from its specific substrate to 2,3,5 triphenyl tetrazolium chloride (TTC), which is reduced, to pink-red colored triphenylformazan (Artenie and Tanase, 1981). The fungal biomass was separated by centrifugation and 2–5 ml of phosphate buffer (pH 7.4) was added according to each sample weight. In the experimental variants, 1 ml of the obtained mixture is supplemented with 0.2 ml of the corresponding enzyme substrate for each of the four dehydrogenases (isocitric acid, ketoglutaric acid, succinic acid, and malic acid), while 0.2 ml of phosphate buffer was introduced into each control tube. The tubes were kept at 28 °C for 24 h. At the end of the incubation time period, in each tube, 5 ml of acetone was added to extract the triphenylformazane resulted by reduction reactions.

The soluble protein content was assayed at 595 nm according to Bradford method (Bradford, 1976) and the assayed enzyme activities were expressed relatively to the protein content. The experiment was repeated twice and rather similar results were obtained; the best correlated data are presented below. The average values resulted from five measurements of each enzyme activity were considered for graphical plots. The ANOVA test was applied, considering the $p < 0.05$ threshold of statistic significance

Table 1
AgNP suspension volumes added in the fungus growth medium.

Sample	C	V1	V2	V3	V4	V5
AgNP suspension	0	200 µl/l	400 µl/l	600 µl/l	800 µl/l	1000 µl/l

for the comparison of means of the control samples and the test ones.

3. Results and discussion

3.1. AgNPs characterization

3.1.1. Electron microscopy data

The TEM imaging (Fig. 1a–d) has provided data on the silver nanoparticle size and morphology, revealing rather symmetrical nanostructures, possibly quasi-spherical or discoidal nanoparticles, with size polydispersity and rare nanosystems of exceptional large dimension.

We mention that, as known, some of particles whose images suggest their association in the studied sample could be also the result of the suspension drop drying after deposition on the support for the electron microscopy investigation.

The most of the visualized particles have rather small sizes as can be seen in Fig. 1a–c and in the dimensional histogram for over 1000 AgNPs (Fig. 1d) that was fitted with log-normal function. According to corresponding histogram, most frequent nanoparticles appeared to be the 5.3 nm ones (Fig. 1b) while other particles with diameters up to 10 nm were also identified. The above results are concordant with those of Vodnik et al. (2008) that evidenced 5

to 6 nm diameter AgNPs and those of Atta et al. (2013) that reported 12–14 nm diameters of citrate-AgNPs, measured by TEM.

SEM investigation carried out on wider scanning field (micrometric scale) has revealed preferentially larger particles like the one surprised in the TEM image presented in Fig. 1c. In Fig. 2a and b the SEM visualizations showed the co-existence of silver nanoparticles having 20–50 nm diameter and quasi-spherical shape as well as associations of couple of large particles (up to 100 nm). Our SEM data are concordant with that of other authors that studied citrate-AgNPs dimensions by SEM (Mazzonello et al., 2017; Raza et al., 2016).

3.1.2. EDX analysis

EDX analysis resulted in the identification of chemical elements that are present in the sample and the estimation of their relative abundance (Table 2 and Fig. 3).

EDX spectra (Fig. 3) shows silver peak indicating the presence of silver nanoparticles along with aluminum (Al) and silicon (Si) and other elements characterizing the sample glass substrate (Table 2) but also with carbon (C) and oxygen (O) present in the citrate capping layers or still unreacted in the suspension.

Silver percentage is very small - which is not surprisingly considering the small concentration of AgNPs in the drop of aqueous
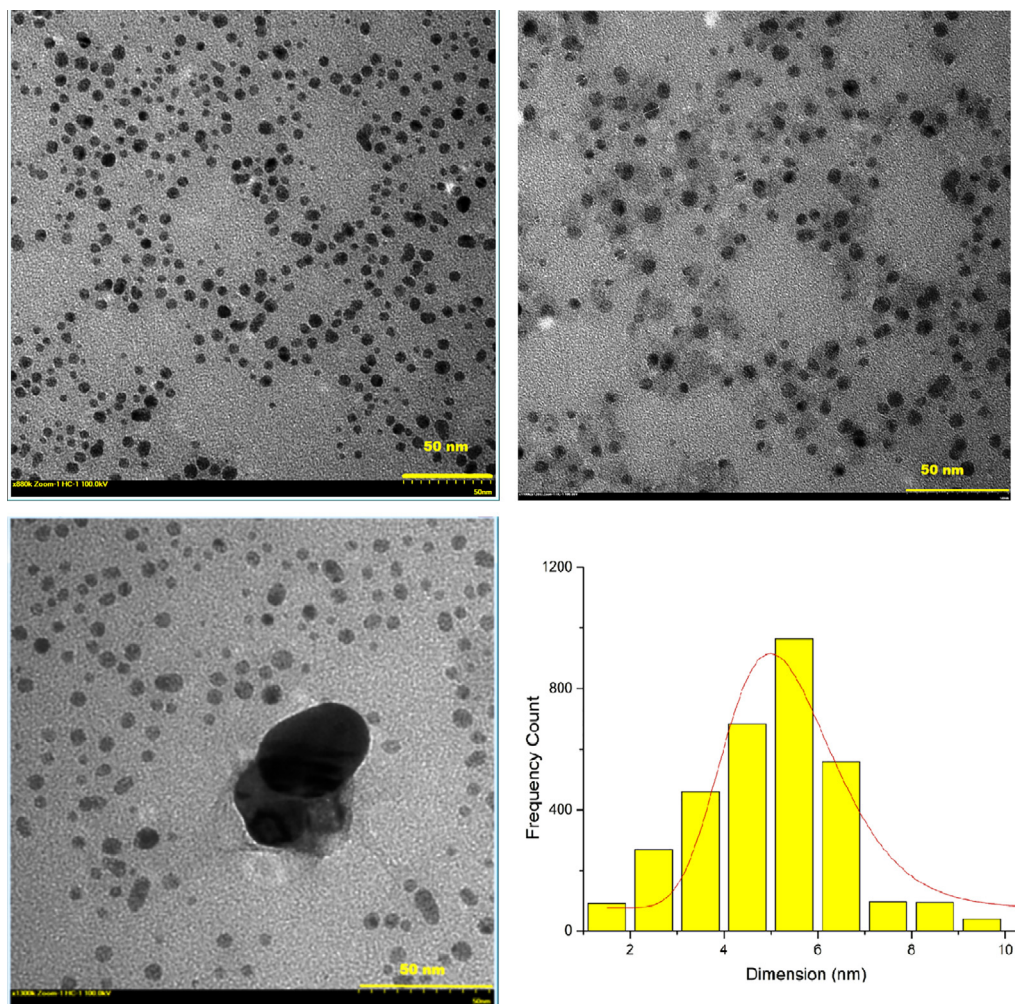
Fig. 1. TEM imaging of freshly prepared AgNP sample. (a) and (b) AgNPs with quasi-spherical shape and of several nm diameter; (c) AgNPs of exceptional large size i.e. about 40 nm, among dominant smaller than 10 nm particle; (d) histogram of AgNPs can be fitted with mathematical function: y = 78.8 + 2478.7 (sqrt(2PI 0.23x) exp(−ln(x/5.26))^2/2 (0.23^2); y-particle size frequency; x-particle size; PI-polydispersity index).
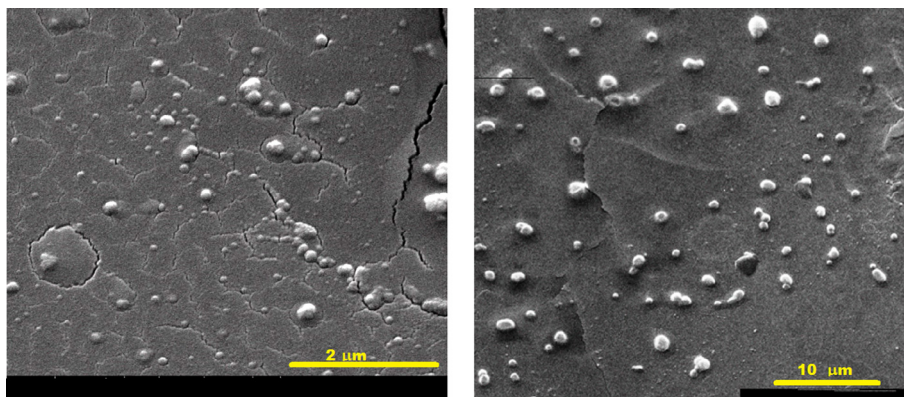
Fig. 2. SEM image of fresh AgNP sample; (a) 2 μm scale bar; (b) 10 μm scale bar.

Table 2
EDX analysis results (Wt-percentage of element weight; At-atom abundance percentage.

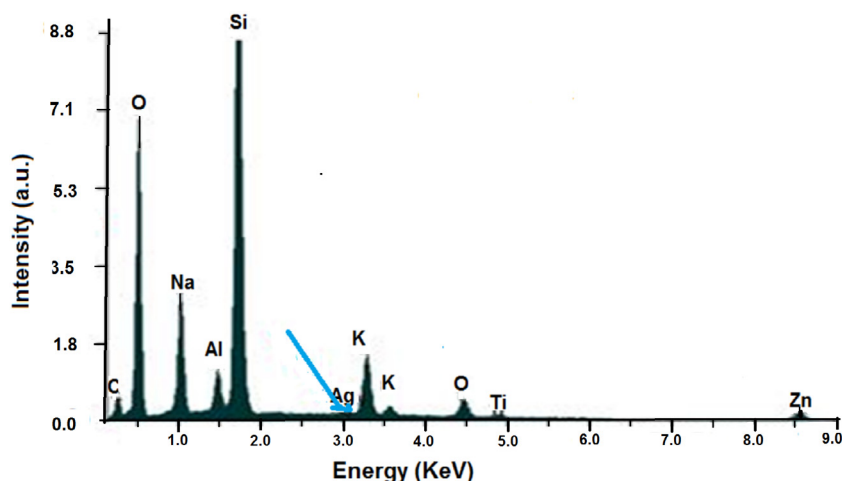| Element/spectral line	CK	OK	NaK	AlK	SiK	AgL	KK	TiK	ZnK
Wt (%)	19.24	49.76	07.72	01.70	17.73	00.08	02.12	00.74	00.91
At (%)	11.95	41.14	09.18	02.37	25.74	00.42	04.28	01.84	03.09

Fig. 3. EDX analysis recording result.

suspension dispersed on the surface of the support exposed to elemental investigation.

3.1.3. SAXS data interpretation

To get more detailed insight into the silver nanoparticle properties we carried out SAXS investigation. Scattering intensity $I(q)$ in average dispersing volume V_i can be written as:

$$I(q) = NV_i^2 \Delta\rho^2 |F(q)|^2 S(q) \qquad (4)$$

where q is the scattering vector, or the momentum transfer vector, $q = 4\pi \sin\theta/\lambda$, ($\lambda$ being the wavelength of the X-rays and θ is half the scattering angle), N is number of scattering centres per cube cm, $\Delta\rho$ is particle-dispersion liquid difference in density; $|F(q)|^2 = P(q)$ is the particle shape factor and $S(q)$ is factor of suspension structure ($S(q) = 1$ for diluted suspensions). For relatively small q domain (Guinier region):

$$I(q) = I(0) \exp\left[-q^2(Rg)^{2/3}\right] \qquad (5)$$

with Rg-the particle giration radius. When q is remarkably large ($q \gg 1/Rg$) then $I(q)$ reflects the characteristics of the interface between suspended particles and dispersion liquid (Porod region); for discoidal particles $I(q)$ is proportional with q^{-2} while for spherical particles $I(q)$ is proportional with q^{-4} (Glatter and Kratky, 1982). Beaucage modeling combines the approaches of Guinier and Porod approaches (Beaucage, 1995, Beaucage et al., 2004) with the shape factor depending on giration radius and the particle/liquid interface:

$$I(q) = G \exp\left(-q^2 Rg^{2/3}\right) + B/q_0^n + y_0 \qquad (6)$$

where $q_0 = f(q, Rg, \varepsilon)$, ($\varepsilon$ = error), G is Guinier factor proportional with particle concentration, B is the factor depending on the power of q in the region of large values of $I(q)$, and y_0 is a coefficient corresponding to incoherent diffusion.

The approach through Beaucage unified model (red curve, Fig. 4) provided good fitting of experimental data (dashed curve).
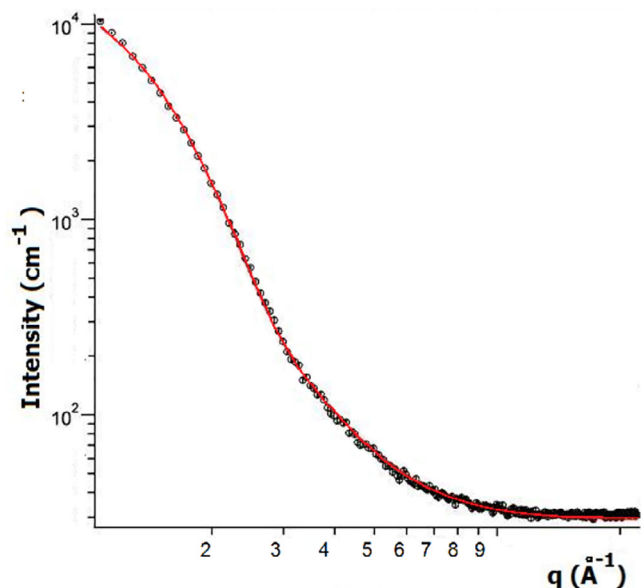
Fig. 4. Scattering curve (log–log plot) and fitting with unified model (Beaucage et al., 2004).

The exponent, n, is always 4 while the other parameters were obtained by iterative calculation (IRENA software). The results of Beaucage unified fitting correlation are: G = 22766; Rg = 151 Å=15.1 nm; B = 0.00017839; P = 4. Statistic analysis according to applied model gave log-normal distribution parameters: σ = 0.278; PDI- poly dispersity index = 2.53.

When $q > 0.02$ Å^{-1} then $I(q)$ was a function of q^{-4}. This is characteristic for particles with smooth surface and negligeable interactions among them. The capillary and solvent backgrounds were subtracted from the original intensity profiles.

For a system with spherical particles obeying log-normal radius distribution, Beaucage approach (Beaucage et al., 2004) gave distribution parameters: R_0 (characteristic radius) and $\cdot\sigma$

$$R_0 = Rg(5/3)^{1/2}\exp(-7\sigma^2) \qquad (7)$$

σ – (ln PDI/12)$^{1/2}$, PDI – poly dispersity index. With (4) one can get the radius R_0 = 11 nm (diameter of about 22 nm).

The AgNP size mathematically estimated by this investigation method reflects implicitly the way it behaves in movement in the surrounding fluid and appears to be larger than in the dried samples characterized by direct TEM method; the data are concordant with the hydrodynamic diameter estimated in Zuo (2014) of about 24 nm.

3.1.4. Optical microscopy data

In DF optical microscopy the visualization of AgNPs is possible due to Localized Surface Plasmon Resonance emission phenomenon that allows imaging of real particles of two orders of magnitude smaller.

In Fig. 5 inset, the size histogram was given, that reveals highest frequency of about 11 nm AgNPs, in agreement with Hansen and Thünemann (2015), not far from the TEM data analysis result. Particle association in dimmers of about 36 nm can be seen in the intensity profiles of light diffracted by dimmers (colored bifurcated curve), dimmers being formed through neighbor particle interaction due to attraction forces, probably favored by local organization of citrate capping layer.

The analysis in UV–Vis spectroscopy has confirmed the phenomenon of Localized Surface Plasmon Resonance evidencing the

corresponding spectral band and its behavior in aged samples and under UV radiation exposure.

3.1.5. Spectral results of citrate-AgNP stability investigation

Fig. 6 shows the UV–VIS spectra of AgNPs, typical for the LSPR band of citrate-silver nanoparticles (Bastús et al., 2014; Alula et al., 2018; Rashid et al., 2013) from the freshly prepared suspension and the aged one, in the range 300–600 nm; they revealed particle polydispersity, with the maximum of the light extinction band at 416 nm (Fig. 6) and respectively at 439 nm.

According to (Hajiesmaeilbaigi et al., 2006) the uncoated AgNPs in water suspension exhibit a LSPR band at about 400 nm, with sharp peak denoting spherical particles.

In the synthesis based on the silver reduction and coating with citrate, a broad LSPR band results, as reported by García-Barrasa et al. (2011) which is red-shifted compared to uncoated ones, suggesting citrate contribution to nanoparticle size increase and polydispersity.

The red-shift of LSPR band from 400 to 416 nm presented by us in Fig. 6 could be caused by particle size increase during storage time period of citrate-AgNPs.

This could be caused by the complex composition of the citrate-AgNP suspension, involving dynamical electric phenomena at the AgNP surface, for example due to silver and sodium ions available for electron acceptance, (Mogensen and Kneipp, 2014). However according to Alzahrani (2017) up to date it was not established any general rule for the LSPR band shift because of numerous factors that could influence that spectral behavior: particle size, shape, dimensional distribution, particle association, but also molecular vicinity – mainly coating shell properties, and suspension composition, reflected especially the pH and the refractive index (Pillai and Kamat, 2004), Badawy et al., 2010). Thus, because of combined actions of such factors there is rather difficult to explain the LSPR band position; according to Campos et al. (2019), in some cases, in citrate coated AgNPs suspension, compared to naked particles in water suspension, there could be observed a blue-shift, while in other, apparently similar cases, there is a red-shift or no band shifting at all.

Attempting to detail the effects of silver reduction with trisodium citrate one needs to take into account the general acceptation of its relatively weak reducing capacity (Agnihotri et al., 2014), thus, it is plausible to figure out that, during long time storage, unreacted citrate ions have associated to each other or with citrate already bound to nanoparticles. In the last situation some bound citrate ions could be taken away from nanoparticle surface allowing the divestment of certain surface spots; at the level of naked particle spots, the neighbor particles attraction could result in some larger size nanosystems (as it was shown by dimmers identified by DF microscopy, Fig. 5).

This process of citrate re-organization and particle association could contribute to red-shift of LSPR band, which is in accord with literature report (Saion et al., 2013), that assigns the red-shift to particle size increasing, while the blue-shift is associated with particle size diminution.

Also, because of the proved weak reduction capacity of citrate, the unreacted silver and citrate ions remained from initial reduction reaction (Yan et al., 2014), are supposed to continue to develop a slow chemical interaction with the continuation of nanoparticle formation during storage time period. In the study presented inhere the four times increase of LSPR band – from about 0.4 to approximately 1.6 intensity (Fig. 6), seems to demonstrate the continuation of nanoparticle synthesis, the dynamical balance between chemical species from citrate-AgNP suspension being pushed toward new nanoparticle formation.

In Fig. 7 the effect of UV ray exposure on the aged AgNP suspension was presented. One can see the progressive increase of SPR
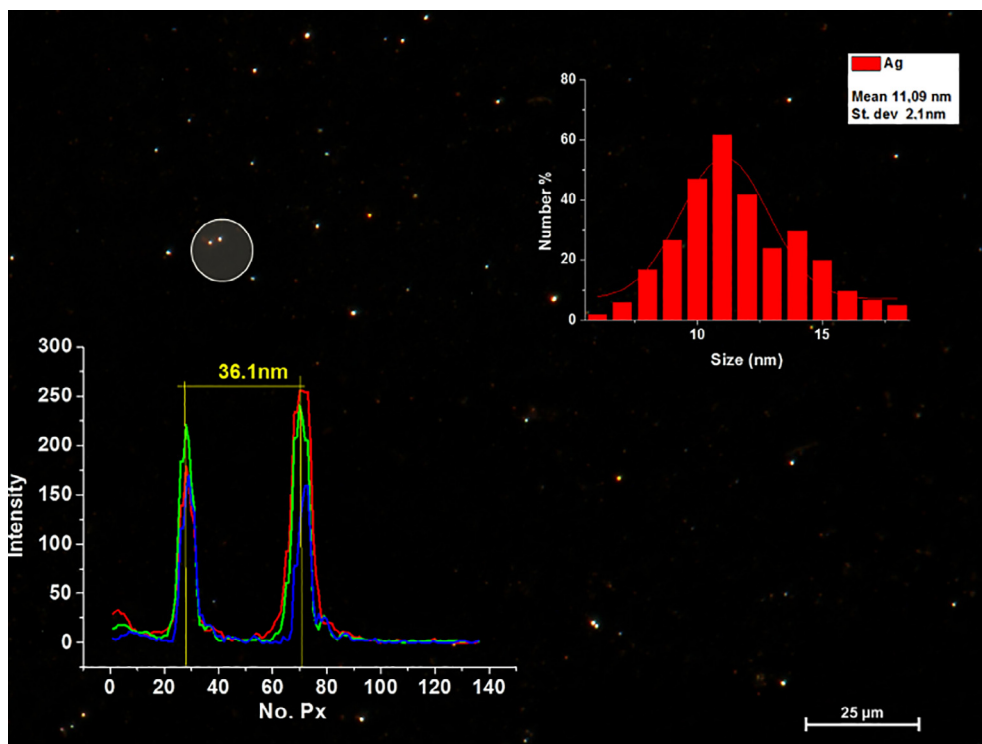
Fig. 5. Dark field (DF) microscopy visualization of AgNPs with diameter histogram and intensity profiles of light diffracted by dimmers; most frequent structures appear to have diameters of about 11 nm while rare dimmers reach 36 nm.
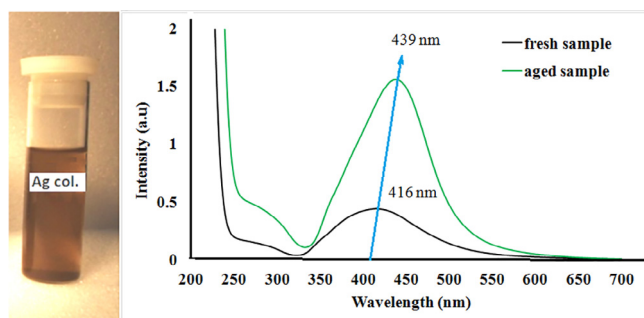
Fig. 6. (left) Photo of colloidal AgNP aged sample; (right) UV–Vis spectra recorded for AgNP freshly prepared and aged samples.
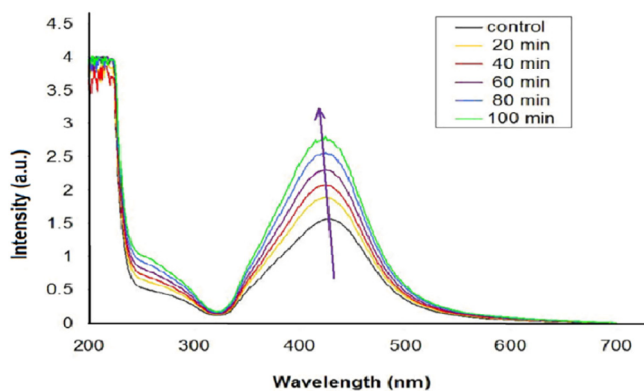
Fig. 7. UV ray exposure effect on the AgNPs in colloidal suspension.

peak intensity from 1.6 to about 2.7 during 100 min of irradiation. Simultaneously slight progressive blue-shift from 439 nm to 435 nm was observed. We mention that sample acidity assessing

has resulted in pH value of about 6 before UV irradiation and about 7.5 after irradiation. In previous studies (Babusca et al., 2020) the analyzed citrate-AgNP suspensions by chemical reduction were prepared and immediately after that they were exposed to UV-C radiation (two step photochemical reduction); there we found the LSPR band intensity increasing from 0.05 after chemical reduction step to 4.5 after UV exposure step, while acidity has changed from the pH of about 5 to approximately 6; also LSPR maximum position was blue-shifted from 425 nm to 418 nm.

In the available literature reports dedicated to AgNPs synthesis by photochemical reduction, UV radiation is generally used simultaneously with the reagent mixing and heating, i.e. there is a one-pot photochemical reduction (Jia et al., 2006; Sato-Berrú et al., 2009). Sato-Berrú et al. (2009) have shown that the use of 356 nm UV rays to assist citrate reduction of silver nitrate for 4 h has led to about three time increase of the LSPR band with not significant peak shift.

The resumed analysis of our results presented in Figs. 6 and 7, suggests that yet after one year of slow reaction in darkness and at low temperature, the exposure to UV radiation at room temperature has emphasized that the studied AgNP suspension still has resources for new nanoparticle formation.

Regarding the pH effect, according to Loiseau et al. (2019) LSPR band appears to be influenced by the pH-dependent redox potential of the corresponding reducer, the citrate, and consequently on the reduction rate of the silver source reagent. Another study showed that the LSPR band was blue-shifted and also the LSPR band intensity was enhanced for the increased pH (Alqadi et al., 2014); in their report the blue-shift and the narrowing of the intense LSPR band was associated with nanoparticles size decreasing.

One might say that the citrate-AgNP suspension synthesized by us behaves as a dynamical colloidal system rather sensitive to UV radiation, even after long time storage in darkness and at low temperature.

3.2. The results of cellulolytic fungi tests

3.2.1. Fungi growth test

The growth of cellulolytic fungus in the presence of freshly prepared AgNP suspension supplied to agarized medium (C – control, V1, V2, V3, V4, V5 – AgNP variants corresponding to 200–400–600–800–1000 µl/l of AgNP suspension) was measured two days after inoculation.

Reduced disk diameters were noticed in AgNP supplied cultures, compared to the control (C) after 48 h – although no mathematically correlated with AgNP suspension concentration (Fig. 8).

3.2.2. Biochemical assay results

3.2.2.1. Antioxidant enzymes. The activities of the two antioxidant enzymes assayed by us in the mycelium samples, the catalase and the superoxide dismutase, in Fig. 9 and Table 3 are given.

In Fig. 9 the levels of catalase activity in the mycelium of *P. chrysosporium* cultures supplied with AgNP suspensions are presented. The representative results, corresponding to 14 day old fungi cultures, showed the net increase of catalase activity from 38 to 60 CAT unit per gram of protein ($p < 0.05$), i.e. the enhanced CAT synthesis manifests as an adaptive response to the oxidative stress induced by silver supply. Still, younger fungi cells, at 7 growth days, present slight diminution of catalase activity (Fig. 9) as possible result of yet inactive adaptation mechanisms or/and as initially rapid increase of total protein synthesis that didn't keep the same rate during next seven days of growth.

It is a clear signal of antioxidant stress induced following AgNP addition to fungus culture medium, that is probably generated by the increased levels of reactive oxygen species (ROS) – since catalase substrate is the hydrogen peroxide, H_2O_2, usually the most frequent such reactive species. One could say that the oxidative stress resulted because of catalytic action of silver that entered the fungi cells in the form of oxidized atoms delivered by AgNP surface or from the free silver ion pool still existing from the dissociated silver salt in the aqueous suspension.

In the presence of solved oxygen, water molecules that are catalytically broken down in hydroxyl and hydrogen free radicals lead to toxic reaction products, mainly hydrogen peroxide, H_2O_2 and superoxide radical, O_2^-, but also many other intermediate products, much more instable and, thus, very difficult to take into discussion.

In Table 3 the data showing the activity of superoxide dismutase (SOD) are presented. The SOD activity values differ quite a
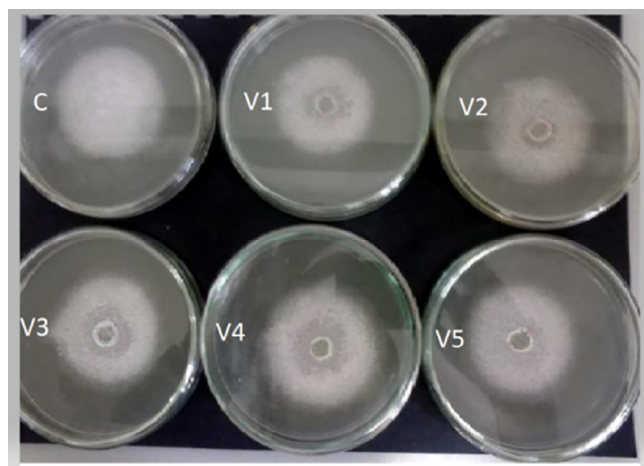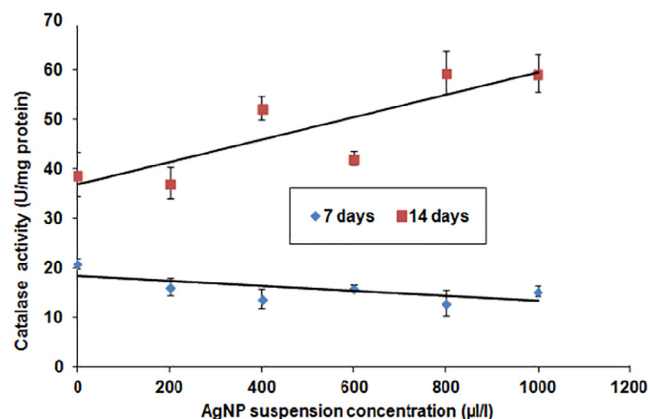

Fig. 9. Catalase activity changes in the studied fungus supplied with AgNP diluted suspensions.

few from the 7th to 14th day old fungus mycelium, with non-monotonous variation, showing a slight increasing trend in the AgNP supplied samples compared to the control ones.

The Anova based mean comparison indicating remarkable variation among the five replies of each tested experimental variants, together with mathematically not correlated SOD values and AgNP suspension concentration, suggests the more complicated processes within fungi cells from the viewpoint of ROS dynamics.

Indeed the superoxide dismutase has as principal substrate the negative ionized molecular oxygen O_2^-, transforming it into neutral, non-toxic O_2 accompanied by reactive hydrogen peroxide, H_2O_2, the catalase substrate which results also from the recombination of water main radicals. In contrast with constant cell responsivity to hydrogen peroxide through CAT biosynthesis mechanisms, it seems that SOD activity adjustment, as response to reactive molecular oxygen, could be influenced by other factors including possible random inactivation within the complex composition of cultivation medium of *P. chrysosporium* fungus when supplied with AgNPs. In Fig. 10 the concentration of malondialdehyde (MDA) is presented, being expressed as nmol per grams of mycelium, and evidencing more pronounced increasing tendency at 7 days of fungus growth ($p < 0.05$), from 77 nmol/g in control samples to about 88 nmol/g for highest AgNP suspension concentration, of 1000 µl/l. These are expectable results since for low catalase action (at 7th day catalase activity was diminished progressively with AgNP increasing concentration (Fig. 9)), the lipid peroxidation (measured by MDA content) could increase with the increasing of AgNP suspension concentration.

Later, at 14th day, when catalase biosynthesis was intensified, protecting fungus tissue against peroxidation reactions, potentially triggered by the hydrogen peroxide, the MDA level appeared almost not changed in comparison to control samples – without AgNPs, but generally increased compared to 7th day sample values. Thus, AgNP supply appears as a source of oxidative stress arousing changes of specific antioxidant enzymes while also other metabolic disturbances could occur too.

3.2.2.2. Krebs' cycle dehydrogenases. The cellulolytic action of *P. chrysosporium* fungus is related to the cellulolytic enzymes released in the environment where wood waste accumulates from natural and industrial sources. Those enzymes are normally produced when an optimal bioenergetics occurs in the fungus cells, with undisturbed Krebs' cycle processes, including dehydrogenases activities; to quantify the four dehydrogenase enzymes, the mycelium of the chosen fungus was analized for the same concentrations of AgNP suspension.


Fig. 8. Photo of *P. chrysosporium* fungus growth in the agarized samples supplied with AgNPs.

Table 3
Superoxide dismutase activity changes in the fungus mycelium.

AgNP suspension (μl/l)	7 days		14 days	
	U/mg of protein	StDev (%)	U/mg of protein	StDev (%)
0	0.95	12.49	0.87	6.14
200	0.56	13.35	0.39	11.08
400	1.17	14.71	1.10	3.79
600	1.07	12.08	0.76	11.17
800	1.07	7.46	1.26	10.26
1000	0.54	8.38	0.89	12.62
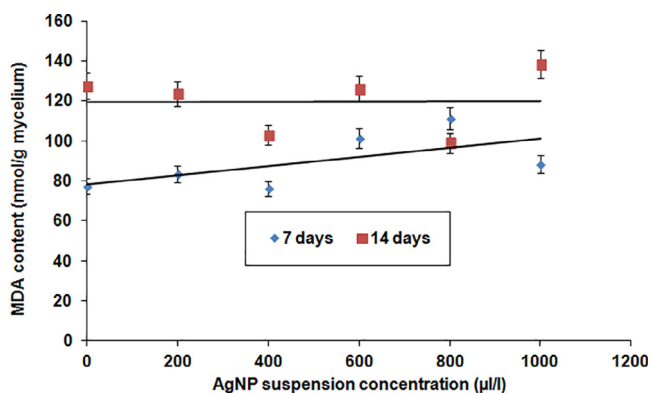
Fig. 10. Malondialdehyde content in the *fungus mycelium* grown with AgNP diluted suspension.
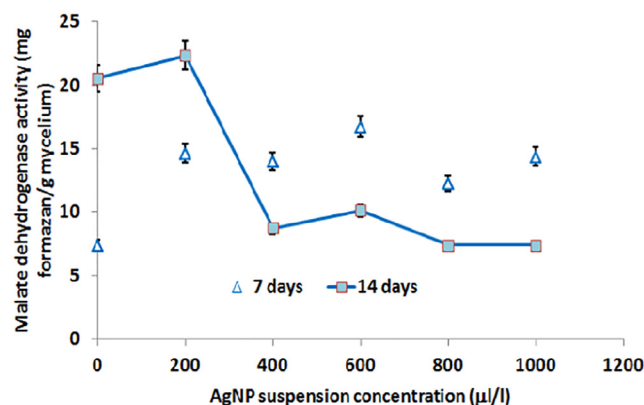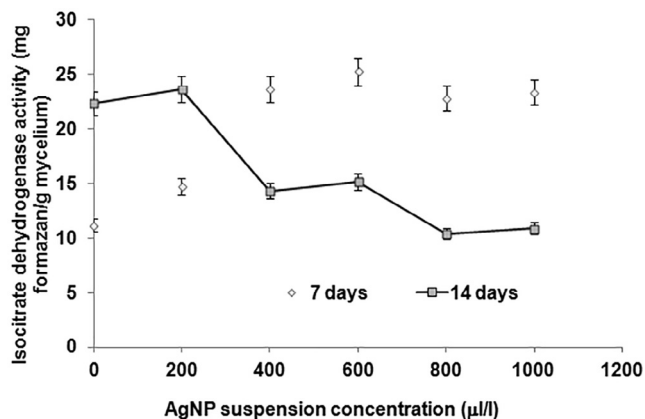
Fig. 11. Succinate dehydrogenase activity in the *fungus mycelium* as result of AgNP supply.

In Fig. 11 the activity of succinate dehydrogenase is presented. While for only 7 days, when relative increase of the enzyme activity was recorded, in the final 14 day old fungus the decrease from about 24 units (mg of formazan per gram of mycelium) to 11 units was recorded – for 400 to 1000 μl/l experimental variants with statistical significance $p < 0.01$. It is probably related to the fact that at 7 days the total protein synthesis was stimulated while at 14 days it was impaired by the supply with silver suspension (data not shown). The smaller diameters of fungus culture in the silver variants compared to the control could suggest this differentiated growth (Fig. 8).

In Fig. 12 the similar behavior of malate dehydrogenase can be seen – the enzyme reversibly catalyzes the reactions of malate oxidization. In the final 14 day old fungal samples the enzyme activity was diminished evidently from over 20 units to less than 8 units, from 200 μl/l to 1000 μl/l experimental variants, in spite of the relative increase in earlier fungi cultures at seven days ($p < 0.01$). Also

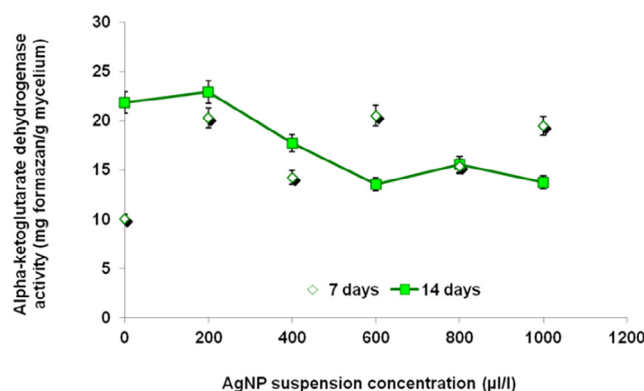**Fig. 12.** Malate dehydrogenase activity in the *fungus mycelium* supplied with AgNPs.

the metabolic disturbances of the studied fungus cells in the presence of silver nanoparticles could be illustrated by the diminution of the activity of alpha-ketoglutarate dehydrogenase (Fig. 13).

The average values (Fig. 13) represented in the graph decreased from about 23 units to around 14 units from 200 μl/l to 1000 μl/l experimental variants ($p < 0.01$).

In the same time in the fungus cells occurred the significant decreasing ($p < 0.01$) of isocitrate dehydrogenase activity following the silver supply (Fig. 14); in 7 day old samples the enzyme activity diminution ranged from about 22 units to around 10 units to the increase of AgNP concentration.

We noticed that, as in the cases of previous enzymes, except-succinate dehydrogenase, slight increase was found for the lowest AgNP concentration (200 μl/l) – but with no statistical significance compared to the control sample data ($p > 0.05$).

We presume that such metabolic impairment as that reflected by the tested dehydrogenases could result because of silver impact

Fig. 13. Alpha-ketoglutarate dehydrogenase activity in the *fungus mycelium* supplied with AgNPs.
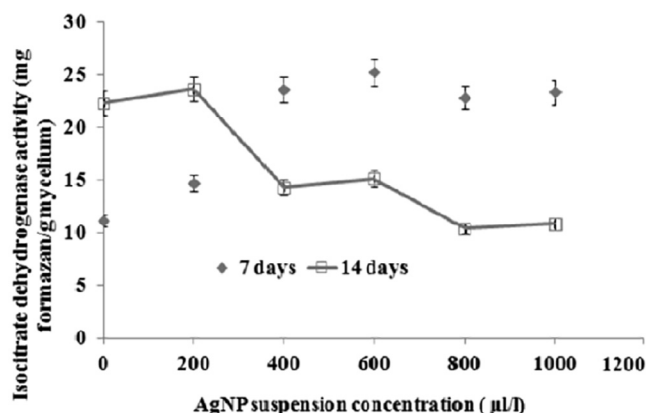
Fig. 14. Isocitrate dehydrogenase activity in the *fungus mycelium* supplied with AgNPs.

in the *fungus mycelium* growth and possibly affect its beneficial role in the environment. The ROS increase evidenced by antioxidant enzyme activity, mainly by CAT activity increase could be the cause of dehydrogenase progressive inactivation to the enhance of AgNP suspension concentration increase.

Further experiments are going to be designed to get new data that could enable us to describe the intimate mechanisms underlying the interaction of fungal cells and the silver nanoparticles. At the present moment we just could suppose that silver enter the fungus cells after being released by endocytosed nanoparticles – as found for 10 nm AgNPs in algae (Sekine, 2017) or silver atoms are released in the vicinity of cellular wall being able to induce a considerable effect following the interaction with Krebs' cycle enzymes.

4. Conclusions

The impact of silver nanoparticles on some environmental beneficial fungus, *Phanerochaete chrysosporium* was evidenced by means of some enzymes activities. We worked with citrate-silver nanoparticles synthesized in the form of fresh colloidal suspensions, that were characterized by good granularity, containing mainly small particles, around 5.6 nm size according to TEM data; they appeared to be accompanied by rare larger particles of tens of nm as confirmed by SEM and SAXS - diameter of about 22 nm; also rare dimmers - of about 36 nm size were evidenced by dark field optical microscopy suggesting the complex interaction phenomena in the colloidal sample.

Sample ageing and exposure to UV-C evidenced the continuation of particle formation –the Localized Surface Plasmon Resonance band intensity increased from about 0.4 to approximately 1.6, during ageing; also the synthesis continuation during ultraviolet radiation impact was remarked since the LSPR band intensity increased from 1.6 to about 2.7 during 100 min of irradiation.

The response of *P. chrysosporium* fungus to AgNP suspension administration has been evidenced by the increase of antioxidant enzyme activity as well by the diminution of some dehydrogenases activities. While catalase activity increasing, from 38 to 60 units, denotes an adaptive behavior to the hydrogen peroxide formation because of silver catalytic action on the aqueous media, the diminution to about 50% of the activities of the four dehydrogenases (malate dehydrogenase, isocitrate dehydrogenase, alpha-ketoglutarate dehydrogenase and succinate dehydrogenase) compared to the control fungal samples, suggests the impairment of metabolic processes.

To search for further consequences of nanosized silver in the fungal mycelium new investigation methods are planned to be applied aiming to elucidate the intimate interactions at the inter-face Ag/fungus cells in the frame of future experimental project.

Declaration of Competing Interest

The authors declare that they have no known competing financial interests or personal relationships that could have appeared to influence the work reported in this paper.

References

Vicky, V.M., Rodney, S., Ajay, S., Hardik, R.M., 2010. Introduction to metallic nanoparticles. J. Pharm. Bioallied Sci. 2 (4), 282–289.

Lee, S.H., Jun, B.-H., 2019. Silver nanoparticles: synthesis and application for nanomedicine. Int. J. Mol. Sci. 20 (4), 865.

Sekine, R., Moore, K.L., Matzke, M., Vallotton, P., Jiang, H., Hughes, G.M., Kirby, J.K., Donner, E., Grovenor, C.R.M., Svendsen, C., Lombi, E., 2017. Complementary imaging of silver nanoparticle interactions with green algae: dark-field microscopy, electron microscopy, and nanoscale secondary ion mass spectrometry. ACS Nano. 11 (11), 10894–10902.

Sharma, V., Sundaramurthy, A., Tiwari, A., Sundramoorthy, A.K., 2018. Graphene nanoplatelets-silver nanorods-polymer based in-situ hybrid electrode for electroanalysis of dopamine and ascorbic acid in biological samples. Appl. Surf. Sci. 449, 558–566.

Chettri, P., Vendamani, V.S., Tripathi, A., Singh, M.K., Pathak, A.P., Tiwari, A., 2017. Green synthesis of silver nanoparticle-reduced graphene oxide using *Psidium guajava* and its application in SERS for the detection of methylene blue. Appl. Surf. Sci. 406, 312–318.

Jeong, S.-H., Choi, H., Kim, J.Y., Lee, T.-W., 2015. Silver-based nanoparticles for Surface Plasmon Resonance in organic optoelectronics. Particle 32 (2), 164–175.

Mahmudin, L., Suharyadi, E., Utomo, A.B.S., Abraha, K., 2015. Optical properties of silver nanoparticles for Surface Plasmon Resonance (SPR)-based biosensor applications. J. Modern Phys. 06 (08), 1071–1076.

Amendola, V., Bakr, O.M., Stellacci, F., 2010. A study of the Surface Plasmon Resonance of silver nanoparticles by the discrete dipole approximation method: effect of shape, size, structure, and assembly. Plasmonics 5 (1), 85–97.

Cao, W., Huang, T., Xu, X.-H.-N., Elsayed-Al, H.E., 2011. Localized surface plasmon resonance of single silver nanoparticles studied by dark-field optical microscopy and spectroscopy. J. Appl. Phys. 109 (3), 034310.

Kelly, F.M., Johnston, J.H., 2011. Colored and functional silver nanoparticle-wool fiber composites. ACS Appl. Mater. Interfaces 3 (4), 1083–1092.

Pietrzak, K., Gutarowska, B., Machnowski, W., Mikołajczyk, U., 2016. Antimicrobial properties of silver nanoparticles misting on cotton fabrics. Textile Res. J. 86 (8), 812–822.

Tylkowski, B., Trojanowska, A., Nowak, M., Marciniak, L., Jastrzab, R., 2017. Applications of silver nanoparticles stabilized and/or immobilized by polymer matrixes. Phys. Sci. Rev., 20170024

Bapat, R.A., Chaubal, T.V., Joshi, C.P., Bapat, P.R., Choudhury, H., Pandey, M., Gorain, B., Kesharwani, P., 2018. An overview of application of silver nanoparticles for biomaterials in dentistry. Mater. Sci. Eng. C 91, 881–898.

Kaur, A., Goyal, D., Kumar, R., 2018. Surfactant mediated interaction of vancomycin with silver nanoparticles. Appl. Surf. Sci. 449, 23–30.

Huang, Z., Zeng, Z., Song, Z., Chen, A., Zeng, G., Xiao, R., He, K., Yuan, L., Li, H., Chen, G., 2020. Antimicrobial efficacy and mechanisms of silver nanoparticles against *Phanerochaete chrysosporium* in the presence of common electrolytes and humic acid. J. Hazard. Mater. 383, 121153.

Al-Zubaidi, S., Al-Ayafi, A., Abdelkader, H., 2019. Biosynthesis, characterization and antifungal activity of silver nanoparticles by *Aspergillus niger* isolate. J. Nanotechnol. Res. 1 (1), 023–036.

Osonga, F.J., Akgul, A., Yazgan, I., Akgul, A., Eshun, G.B., Sakhaee, L., Sadik, O.A., 2020. Size and shape-dependent antimicrobial activities of silver and gold nanoparticles: a model study as potential fungicides. Molecules 25 (1), 2682.

Bernardo-Mazariegos, E., Valdez-Salas, B., González-Mendoza, D., Abdelmoteleb, A., Tzintzun Camacho, O., Ceceña Duran, C., Gutiérrez-Miceli, F., 2019. Silver nanoparticles from Justicia spicigera and their antimicrobial potentialities in the biocontrol of foodborne bacteria and phytopathogenic fungi. Rev. Argent. Microbiol. 51 (2), 103–109.

Ivask, A., Elbadawy, A., Kaweeteerawat, C., Boren, D., Fischer, H., Ji, Z., Chang, C.H., Liu, R., Tolaymat, T., Telesca, D., Zink, J.I., Cohen, Y., Holden, P.A., Godwin, H.A., 2014. Toxicity mechanisms in *Escherichia coli* vary for silver nanoparticles and differ from ionic silver. ACS Nano 8 (1), 374–386.

Calderón-Jiménez, B., Johnson, M.E., Montoro Bustos, A.R., Murphy, K.E., Winchester, M.R., Vega Baudrit, J.R., 2017. Silver nanoparticles: technological advances, societal impacts, and metrological challenges. Front. Chem. 5, 6.

Kobashigawa, J.M., Robles, C.A., Martínez Ricci, M.L., Carmarán, C.C., 2019. Influence of strong bases on the synthesis of silver nanoparticles (AgNPs) using the ligninolytic fungi Trametes trogii. Saudi J. Biol. Sci. 26, 1331–1337.

Kasprowicz, M.J., Koziol, M., Gorczyca, A., 2010. The effect of silver nanoparticles on phytopathogenic spores of Fusarium culmorum. Can. J. Microbiol. 56 (3), 247–253.

Alananbeh, K.M., Al-Refaee, W.J., Al-Qodah, Z., 2017. Antifungal effect of silver nanoparticles on selected fungi isolated from raw and waste water. Ind. J Pharm. Sci. 79 (4), 559–567.

Gutierrez, R.M., Socorro, M., Daupan, M., Fabian, A.V., Miclat, C.C., 2015. Microbiological investigation on some biodegradable plastics used as packaging materials. Asian J. Appl. Sci. 03 (01), 75–81.

Yi, F., Chen, G., Zeng, G., Guo, Z., Liu, W., Huang, Z., He, K., Hu, L., 2016. Influence of cysteine and bovine serum albumin on silver nanoparticle stability, dissolution, and toxicity to Phanerochaete chrysosporium. RSC Adv. 6, 108.

Huang, Z., Chen, G., Zeng, G., Guo, Z., He, K., Hu, L., Wu, J., Zhang, L., Zhu, Y., Song, Z., 2017. Toxicity mechanisms and synergies of silver nanoparticles in 2,4-dichlorophenol degradation by Phanerochaete chrysosporium. J. Hazard. Mater. 321, 37–46.

Huang, Z., He, K., Song, Z., Zeng, G., Chen, A., Yuan, L., Li, H., Hu, L., Guo, Z., Chen, G., 2018. Antioxidative response of Phanerochaete chrysosporium against silver nanoparticle-induced toxicity and its potential mechanism. Chemosphere 211, 573–583.

Mittelman, A.M., Fortner, J.D., Pennell, K.D., 2015. Effects of ultraviolet light on silver nanoparticle and dissolution. Environ. Sci. Nano 2, 683–691.

Lee, P.C., Meisel, D., 1982. Adsorption and surface-enhanced Raman of dyes on silver and gold sols. J. Phys. Chem. 86 (17), 3391–3395.

Silva, E.I., Rivas, J., Leon, L.M., Isidro, M.A., Lopez, Q., 2007. Synthesis of silver-coated magnetite nanoparticles. J. Non-Crystalline Solids 353, 829–831.

Sasges, M., Robinson, J., Daynouri, F., 2012. Ultraviolet lamp output measurement: a concise derivation of the Keitz equation. Ozone: Sci. Eng. 34 (4), 306–309.

Lawal, O., Dussert, B., Howarth, C., Platzer, K., Sasges, M., Muller, J., Whitby, E., Stowe, R., Adam, W., Witham, D., Engel, S., Posy, P., van der Pol, A., 2017. Method for the Measurement of the Output of Monochromatic (254 nm) Low-Pressure UV Lamps. IUVA News, Spring.

Ilavsky, J., Jemian, P.R., 2009. Irena: tool suite for modeling and analysis of small-angle scattering. J. Appl. Cryst. 42 (2), 347–353.

Manoliu, A., Balan, M., Oprica, L., Gradinaru, P., 2010. The evolution of catalase and peroxidase activity in Phanerochaete chrysosporium grown on media containing beech and fir sawdust and under the influence of some amino acids. Sci. Ann. "Alexandru Ioan Cuza" Univ., Iaşi, Romania. Gen. Mol. Biol. 6, 47–52.

Sinha, A.K., 1972. Colorimetric assay of catalase. Anal. Biochem. 47 (2), 389–394.

Winterbourn, C.C., Hawkins, R.E., Brian, M., Carrell, R.W., 1975. The estimation of red cell superoxide dismutase activity. J. Lab. Clin. Med. 85 (2), 337–341.

Hodges, D.M., DeLong, J.M., Forney, C.F., Prange, R.K., 1999. Improving the thiobarbituric acid-reactive-substances assay for estimating lipid peroxidation in plant tissues containing anthocyanin and other interfering compounds. Planta 207 (4), 604–611.

Artenie, V., Tanase, E., 1981. Practicum de biochimie generala (in Romanian). Editura Univ Al. I Cuza, Iasi, Romania, pp. 233–239.

Bradford, M., 1976. A rapid and sensitive method for the quantification of microgram quantities of protein utilizing the principle of protein-dye binding. Analyt. Biochem. 72 (1–2), 248–254.

Vodnik, V.V., Božani, D.K., Bibi, N., Šaponji, Z.V., Nedeljkovi, J.M., 2008. Optical properties of shaped silver nanoparticles. J. Nanosci. Nanotechnol. 8 (7), 3511–3515.

Atta, A.M., Al-Lohedan, H.A., EL-Mahdy, G.A., Ezzat, A.R.O., 2013. Application of stabilized silver nanoparticles as thin films as corrosion inhibitors for carbon steel alloy in 1 M hydrochloric Acid. J. Nanomater. 5, 1–8.

Mazzonello, A., Valdramidis, V.V., Farrugia, C., Grima, J.N., Gatt, R., 2017. Synthesis and characterization of silver nanoparticles. Int. J. Modern Eng. Res. 7 (3), 41–47.

Raza, M.A., Kanwal, Z., Rauf, A., Sabri, A.N., Riaz, S., Naseem, S., 2016. Size-and shape-dependent antibacterial studies of silver nanoparticles synthesized by wet chemical routes. Nanomaterials (Basel) 6 (4), 74.

Hansen, U., Thünemann, A.F., 2015. Characterization of silver nanoparticles in cell culture medium containing fetal bovine serum. Langmuir 31 (24), 6842–6852.

Bastús, N.G., Merkoçi, F., Piella, J., Puntes, V., 2014. Synthesis of highly monodisperse citrate-stabilized silver nanoparticles of up to 200 nm: kinetic control and catalytic properties. Chem. Mater. 26 (9), 2836–2846.

Alula, M.T., Karamchand, L., Hendricks, N.R., Blackburn, J.M., 2018. Citrate-capped silver nanoparticles as a probe for sensitive and selective colorimetric and spectrophotometric sensing of creatinine in human urine. Anal. Chim. Acta 1007, 40–49.

Rashid, M.U., Bhuiyan, M.K.H., Quayum, M.E., 2013. Synthesis of silver nano particles (Ag-NPs) and their uses for quantitative analysis of vitamin C tablets. Dhaka Univ. J. Pharm. Sci. 12 (1), 29–33.

Hajiesmaeilbaigi, F., Mohammadalipour, A., Sabbaghzadeh, J., Hoseinkhani, S., Fallah, H.R., 2006. Preparation of silver nanoparticles by laser ablation andfragmentation in pure water. Laser Phys. Lett. 3 (5), 252.

García-Barrasa, J., López-de-Luzuriaga, J.M., Monge, M., 2011. Silver nanoparticles: synthesis through chemical methods in solution and biomedical applications. Cent. Eur. J. Chem. 9 (1), 19.

Mogensen, K.B., Kneipp, K., 2014. Size-dependent shifts of plasmon resonance in silver nanoparticle films using controlled dissolution: monitoring the onset of surface screening effects. J. Phys. Chem. C 118 (48), 28075–28083.

Alzahrani, E., 2017. Colorimetric detection based on localized surface plasmon resonance optical characteristics for the detection of hydrogen peroxide using acacia gum–stabilised silver nanoparticles. Anal. Chem. Insights 12. 1177390116684686.

Pillai, Z.S., Kamat, P.V., 2004. What factors control the size and shape of silver nanoparticles in the citrate ion reduction method?. J. Phys. Chem. B. 108, 945–951.

Badawy, A.M.E., Luxton, T.P., Silva, R.G., Scheckel, K.G., Suidan, M.T., Tolaymat, T.M., 2010. Impact of environmental conditions (pH, ionic strength, and electrolyte type) on the surface charge and aggregation of silver nanoparticles suspensions. Environ. Sci. Technol. 44, 1260–1266.

Campos, A., Troc, N., Cottancin, E., Pellarin, M., Weissker, H.-C., Lermé, J., Kociak, M., Hillenkamp, M., 2019. Plasmonic quantum size effects in silver nanoparticles are dominated by interfaces and local environments. Nature Phys. 15, 275.

Yan, S., Wu, Z., Yu, H., Gong, Y., Tan, Y., Du, R., Chen, W., Xing, X., Mo, G., Chen, Z., Cai, Q., Sun, D., 2014. Time-resolved small-angle X-ray scattering study on the growth behavior of silver nanoparticles. J. Phys. Chem. C 118 (21), 11454–11463.

Agnihotri, S., Mukherji, S., Mukherji, S., 2014. Size-controlled silver nanoparticles synthesized over the range 5–100 nm using the same protocol and their antibacterial efficacy. RSC Adv. 4, 3974.

Saion, E., Gharibshahi, E., Naghavi, K., 2013. Size-controlled and optical properties of monodispersed silver nanoparticles synthesized by the radiolytic reduction method. Int. J. Mol. Sci. 4, 7880–7896.

Babusca, D., Popescu, L., Sacarescu, L., Dorohoi, D.O., Creanga, D., Oprica, L.A., 2020. Two phase photochemical synthesis of silver nanoparticles and their impact on the chlorophylls. Mol. Cryst. Liq. Cryst. 698 (1), 56–64.

Jia, H., Zeng, J., Song, W., An, J., Zhao, B., 2006. Preparation of silver nanoparticles by photo-reduction for surface-enhanced Raman scattering. Thin Solid Films 2, 281–287.

Sato-Berrú, R., Redón, R., Vázquez-Olmos, A., Saniger, J.M., 2009. Silver nanoparticles synthesized by direct photoreduction of metal salts. Application in surface-enhanced Raman spectroscopy. J. Raman Spectrosc. 40, 376.

Loiseau, A., Asila, V., Boitel-Aullen, G., Lam, M., Salmain, M., Boujday, S., 2019. Silver-based plasmonic nanoparticles for and their use in biosensing. Biosensors 9 (2), 78.

Alqadi, M., Noqtah, O.A., Alzoubi, F., Alzouby, J., Aljarrah, K., 2014. pH effect on the aggregation of silver nanoparticles synthesized by chemical reduction. Mater. Sci.-Pol. 32, 107–111.

Glatter, O., Kratky, O. (Eds.), 1982. Small Angle X-ray Scattering. Academic Press, London.

Beaucage, G., 1995. Approximations leading to a unified exponential/power-law approach to small-angle scattering. J. Appl. Cryst. 28, 717–728.

Beaucage, G., Kammler, H.K., Pratsinis, S.E., 2004. Particle size distributions from small-angle scattering using global scattering functions. J. Appl. Cryst. 37, 523–535.

Zhao, X., Zhou, L., Riaz Rajoka, M.S., Yan, L., Jiang, C., Shao, D., Zhu, J., Shi, J., Huang, Q., Yan, H., Jin, M., 2018. Fungal silver nanoparticles: synthesis, application and challenges. Crit. Rev. Biotechnol. 38 (6), 817–835.

Vigneshwaran, N., Ashtaputre, N., Varadarajan, P., Nachane, R., Paralikar, K., Balasubramanya, R., 2007. Biological synthesis of silver nanoparticles using the fungus Aspergillus flavus. Mater Lett. 61, 1413–1418.

Vahabi, K., Mansoori, G.A., Karimi, S., 2011. Biosynthesis of silver nanoparticles by fungus Trichoderma reesei (a route for large-scale production of AgNPs). Insci. J. 1 (1), 65–79.

Zuo, Y.Chen, G., Zeng, G., Tan, Q., 2014. Transport, fate, and stimulating impact of silver nanoparticles on the removal of Cd(II) by Phanerochaete chrysosporium in aqueous solutions. J. Hazard. Mater. 285C, 236–244.